AGU PUBLICATIONS

JGR

Journal of Geophysical Research: Space Physics

RESEARCH ARTICLE
10.1002/2015JA021041

Key Points:
- Fast magnetosonic waves driven by shell-type proton velocity distributions
- Full kinetic linear theory instability
- Comparison between linear theory and particle-in-cell simulations

Correspondence to:
K. Min,
kmin@auburn.edu

Citation:
Min, K., and K. Liu (2015), Fast magnetosonic waves driven by shell velocity distributions, *J. Geophys. Res. Space Physics*, *120*, 2739–2753, doi:10.1002/(ISSN)2169-9402.

Received 21 JAN 2015
Accepted 16 MAR 2015
Accepted article online 19 MAR 2015
Published online 18 APR 2015

Fast magnetosonic waves driven by shell velocity distributions

Kyungguk Min[1] and Kaijun Liu[1]

[1]Department of Physics, Auburn University, Auburn, Alabama, USA

Abstract Using linear dispersion theory and particle-in-cell simulations, we explore the ion Bernstein instability driven by the shell-type ion velocity distribution which is related to the excitation of fast magnetosonic waves in the terrestrial magnetosphere. We first demonstrate a novel idea to construct the shell velocity distribution out of multiple Maxwellian ring-beam velocity distributions. Applying this technique, we find that the convergence of the linear theory instability can be achieved with only a moderate number of ring-beam components. In order to prove that such an approximation is legitimate and the linear theory instabilities evaluated are indeed valid, we use the exact shell distribution to carry out a number of one dimensional particle-in-cell simulations corresponding to multiple wave propagation angles adjacent to the direction at which the most unstable waves are expected to grow. The agreement between the linear dispersion analysis and the simulation results is generally very good: enhanced waves are organized along the linear theory dispersion curves in the frequency-wave number space, and relative wave amplitudes are ordered as the linear theory growth rates very well. However, the simulations show a few extra branches that are not expected from the linear dispersion analysis. A close examination of these extra branches suggests that they are not simulation artifacts and particularly related to the ring/shell-type distributions with large ring/shell speed ($v > \sim 1.5\, v_A$, where v_A is the Alfvén speed). In addition, our results show that substantial wave growth can occur at nonintegral harmonics of the proton cyclotron frequency at wave normal angles substantially far away from the perpendicular direction, which may provide an alternative explanation of the off-harmonic peaks of some fast magnetosonic waves observed in space.

1. Introduction

Fast magnetosonic waves in the magnetosphere, also called "equatorial noise" when first observed [*Russell et al.*, 1970], are characterized with enhanced field fluctuations peaked at harmonics of the proton cyclotron frequency [*Russell et al.*, 1970; *Perraut et al.*, 1982; *Santolík et al.*, 2002]. Theoretical studies showed that these waves are driven by the proton distributions with $\partial f(v_\parallel \approx 0, v_\perp)/\partial v_\perp > 0$ [*Gul'elmi et al.*, 1975; *Perraut et al.*, 1982; *McClements et al.*, 1994; *Horne et al.*, 2000; *Chen et al.*, 2010; *Gary et al.*, 2010], where $f(v_\parallel, v_\perp)$ is the velocity distribution function and $v_\parallel$ ($v_\perp$) denotes the velocity parallel (perpendicular) to the background magnetic field. Such distributions, generally represented by the ring or shell distributions, are observed in various plasma environments [*Freund and Wu*, 1988; *Cottrell and Dendy*, 1988; *Dendy and McClements*, 1993; *Janhunen et al.*, 2003; *Broughton et al.*, 2008; *Meredith et al.*, 2008; *Denton et al.*, 2010]. Here, the "ring" distribution forms a ring of particles in the two-dimensional perpendicular velocity space, $\mathbf{v}_\perp$, but an island in the $v_\parallel - v_\perp$ space, and the "shell" distribution forms a spherical shell of particles in the velocity space, where $v_\perp = |\mathbf{v}_\perp|$ [*Umeda et al.*, 2012].

Observations of the fast magnetosonic waves show that the magnetic field fluctuations are polarized along the background magnetic field [*Perraut et al.*, 1982] and the ratio of the electric field intensity to the magnetic field intensity is in good agreement with the whistler-mode branch of the cold plasma dispersion relation at wave propagation near the direction perpendicular to the background magnetic field [*Boardsen et al.*, 1992]. On the other hand, in plasma conditions substantially deviating from those in the terrestrial magnetosphere where a cold dense background plasma is dominant, the waves occur away from the cold plasma dispersion relation and are akin to ion Bernstein waves [*Denton et al.*, 2010; *Gary et al.*, 2010, 2011; *Liu et al.*, 2011]. To emphasize that the analyses herein are not limited to a specific plasma condition, the more general term "ion Bernstein instability" is used to describe the instabilities driven by the proton velocity distributions possessing $\partial f(v_\parallel \approx 0, v_\perp)/\partial v_\perp > 0$ throughout the paper and the term "fast magnetosonic waves" is used to refer to the ion Bernstein waves occurring close to the cold plasma dispersion relation.

Linear dispersion analysis is a powerful tool to study plasma instabilities driven by free energy sources possessed by the velocity distributions and provides essential guidelines to effectively carry out kinetic

simulations and to interpret the simulated wave characteristics. To examine the linear instabilities arising from $\partial f/\partial v_\perp > 0$, many studies have modeled the underlying velocity distributions with subtracted Maxwellian distributions [*Denton et al.*, 2010; *Gary et al.*, 2010], loss cone distributions [*Horne et al.*, 2000], or Dirac delta (δ)-function distributions [*Perraut et al.*, 1982] due to mathematical simplicity, well-established formulation, and readily available dispersion solvers. These can, however, cover only a subset of the whole parameter space. In contrast, ring and shell velocity distributions provide more flexibility to model the underlying distributions and thus broaden the parameter space to be examined, but the dispersion analysis for these distributions is numerically more demanding because there is no closed-form expression for the integrals of ring and shell distribution functions over $v_\perp$ involved in the dispersion relation [*Umeda et al.*, 2012].

Nevertheless, several studies have employed numerical integration techniques to examine plasma instabilities driven by the ring velocity distribution [*McClements et al.*, 1994; *Umeda et al.*, 2007; *Umeda*, 2007]. One of the most general formulations has been provided by *Umeda et al.* [2012] who, applying the formulation to the analysis of electrostatic electron cyclotron harmonic waves driven by the ring distribution of electrons, showed that the linear instabilities and simulated waves have excellent agreement. On the other hand, the fully kinetic description of instabilities driven by the shell velocity distributions has only been explored using the subtracted Maxwellian distributions [e.g., *Gary et al.*, 2010; *Liu et al.*, 2011] which can model only moderately positive slopes in $f(v_\parallel \approx 0, v_\perp)$ due to the requirement of the nonnegative distribution function and does not allow independent adjustment of the shell speed and the thermal spread [*Liu et al.*, 2011]. The reason may be that unlike the ring distribution that can be separated into the parallel and perpendicular components (i.e., $f_r = g(v_\parallel)h(v_\perp)$), the dispersion relation for a shell distribution requires a numerical integration along both $v_\parallel$ and $v_\perp$.

Inspired by the approach taken by *Umeda et al.* [2012] and aspiring to better understand detailed physics of the recent simulation study of the ion Bernstein instability by *Liu et al.* [2011], we here employ a novel idea to construct the shell velocity distribution out of multiple ring-beam velocity distributions. Subsequently, we use the formulation given by *Umeda et al.* [2012] (referred to as Paper 1 hereinafter) for ring-beam distributions to construct a dispersion solver for shell distributions. Utilizing the new dispersion solver, we revisit the study of *Liu et al.* [2011] (referred to as Paper 2 hereinafter) to examine the ion Bernstein instability driven by the proton shell distribution.

Paper 2 carried out two 2-dimensional (2-D; two spatial dimensions but with three velocity components retained) particle-in-cell (PIC) simulations, called Case I and Case II, respectively, to investigate the ion Bernstein instability arising, respectively, from two different shell velocity distributions. The velocity distribution of Case I, which has a smaller shell speed and larger shell density, was modeled by a subtracted Maxwellian velocity distribution. The corresponding linear dispersion analysis was performed using a well-established dispersion solver based on bi-Maxwellian distributions developed by *Gary* [1993]. In contrast, the velocity distribution of Case II, which has a larger shell speed and smaller shell density, could not be easily modeled by the subtracted Maxwellian distribution due to the large shell speed and small thermal spread of the shell, and consequently, they had to find the right simulation parameters by a trial-and-error approach and examine the enhanced waves via the simulation only. In the present study, we will apply our newly developed dispersion solver to both Case I and Case II in Paper 2 to solve the fully kinetic dispersion equation. The results will be validated against the results in Paper 2 as well as 1-D, high-spatial-resolution PIC simulations corresponding to various propagation angles near the direction of the most unstable modes.

The paper is organized as follows. Section 2 describes how to construct a shell velocity distribution out of multiple ring-beam distributions and, subsequently, the new dispersion solver developed. In section 3 we calculate the dispersion relation for Case I and compare the result with that of Paper 2, and in section 4 we calculate the dispersion relation for Case II and compare the result against the simulated waves for various propagation angles. Section 5 summarizes the results and discusses a few unexpected aspects we have encountered in this study.

2. Shell Velocity Distribution and the Dispersion Solver

The shell velocity distribution used for Case II in Paper 2 can be written as

$$f_s(\theta, v_s, v) = \frac{1}{C_s} \exp\left(\frac{-(v - v_s)^2}{\theta^2}\right), \tag{1}$$

where v_s and θ are the shell velocity and the thermal spread of the shell, respectively, and C_s is the normalization constant

$$C_s = \pi\theta^3\left[2\exp\left(-\frac{v_s^2}{\theta^2}\right)\frac{v_s}{\theta} + \sqrt{\pi}\left(2\frac{v_s^2}{\theta^2}+1\right)\left(1+\mathrm{erf}\left(\frac{v_s}{\theta}\right)\right)\right]$$

such that $\int_0^\infty 4\pi v^2 \mathrm{d}v f_s = 1$. On the other hand, the Maxwellian ring-beam velocity distribution that is the basis of the formulation in Paper 1 can be written as

$$\begin{aligned} f_r\left(\theta_\parallel, v_d, \theta_\perp, v_r, v_\parallel, v_\perp\right) &= f_\parallel\left(\theta_\parallel, v_d, v_\parallel\right) f_\perp\left(\theta_\perp, v_r, v_\perp\right), \\ f_\parallel(\theta_\parallel, v_d, v_\parallel) &= \frac{1}{\sqrt{\pi}\theta_\parallel}\exp\left(-\frac{(v_\parallel - v_d)^2}{\theta_\parallel^2}\right), \\ f_\perp(\theta_\perp, v_r, v_\perp) &= \frac{1}{\pi\theta_\perp^2 C_r}\exp\left(-\frac{(v_\perp - v_r)^2}{\theta_\perp^2}\right), \\ C_r(\theta_\perp, v_r) &= \exp\left(-\frac{v_r^2}{\theta_\perp^2}\right) + \sqrt{\pi}\frac{v_r}{\theta_\perp}\,\mathrm{erfc}\left(-\frac{v_r}{\theta_\perp}\right), \end{aligned} \tag{2}$$

where v_d, $\theta_\parallel$, v_r, and $\theta_\perp$ are the parallel drift velocity, parallel thermal spread, perpendicular ring velocity, and perpendicular thermal spread, respectively, and the normalization constant C_r ensures $\int_{-\infty}^{\infty}\mathrm{d}v_\parallel\int_0^\infty 2\pi v_\perp \mathrm{d}v_\perp f_r = 1$.

It is important to note that any velocity distribution function can be represented by superposition of an infinite number of δ-functions:

$$f_{\mathrm{any}}(v_\parallel, v_\perp) = \int_{-\infty}^{\infty}\mathrm{d}v'_\parallel\int_0^\infty 2\pi v'_\perp \mathrm{d}v'_\perp f_\delta\left(v_\parallel, v_\perp, v'_\parallel, v'_\perp\right) f_{\mathrm{any}}(v'_\parallel, v'_\perp), \tag{3}$$

where we have assumed that f_{any} is gyrotropic and

$$f_\delta\left(v_d, v_r, v_\parallel, v_\perp\right) = \delta(v_\parallel - v_d)\frac{\delta(v_\perp - v_r)}{2\pi v_r}. \tag{4}$$

In the limit of vanishingly small thermal spread, the Maxwellian ring-beam distribution of equation (2) converges to a δ-function of equation (4) since $\lim_{\theta_\parallel\to 0} f_\parallel(\theta_\parallel, v_d, v_\parallel) = \delta(v_\parallel - v_d)$ and $\lim_{\theta_\perp\to 0} f_\perp(\theta_\perp, v_r, v_\perp) = \delta(v_\perp - v_r)/(2\pi v_r)$ [e.g., *Arfken et al.*, 2013, p. 84]. This suggests that one can approximate f_{any} by replacing the integrals in equation (3) with summations and f_δ with f_r, giving the following approximation:

$$\begin{aligned} f_{\mathrm{any}}(v_\parallel, v_\perp) &\approx \sum_{p=-\infty}^{\infty}\sum_{q=0}^{\infty}\eta_{p,q} f_r\left(\theta_\parallel, p\Delta v'_\parallel, \theta_\perp, q\Delta v'_\perp, v_\parallel, v_\perp\right), \\ \eta_{p,q} &= \Delta V f_{\mathrm{any}}\left(p\Delta v'_\parallel, q\Delta v'_\perp\right), \end{aligned} \tag{5}$$

where $\Delta V = 2\pi q\Delta v'_\parallel \Delta v'^2_\perp$ is a finite volume element at $v'_\parallel = p\Delta v'_\parallel$ and $v'_\perp = q\Delta v'_\perp$. Note that $\eta_{p,q}$ represents the relative contribution of an individual Maxwellian ring-beam component. Furthermore, one can use the fact that $\sum_{p,q}\eta_{p,q} = 1$ to get

$$\eta_{p,q} = \frac{f_{\mathrm{any}}\left(p\Delta v'_\parallel, q\Delta v'_\perp\right) C_r(\theta_\perp, q\Delta v'_\perp)}{\sum_{r,s} f_{\mathrm{any}}\left(r\Delta v'_\parallel, s\Delta v'_\perp\right) C_r\left(\theta_\perp, s\Delta v'_\perp\right)}.$$

Since $\theta_\parallel$ and $\theta_\perp$ determine the width of the ring-beam, they can be chosen to be near $\Delta v'_\parallel$ and $\Delta v'_\perp$, respectively. Assuming that f_{any} approaches zero at and beyond some finite velocity $v_{\parallel,\max}$ and $v_{\perp,\max}$ such that $f_{\mathrm{any}}(|v_\parallel| \geq v_{\parallel,\max}, v_\perp) = f_{\mathrm{any}}(v_\parallel, v_\perp \geq v_{\perp,\max}) = 0$ for any $v_\parallel$ and $v_\perp$, one can terminate the summations in equation (5) at $p = \pm p_{\max}$ and $q = q_{\max}$, resulting in the following approximation:

$$f_{\mathrm{any}}(v_\parallel, v_\perp) \approx \sum_{p=-p_{\max}}^{p_{\max}}\sum_{q=0}^{q_{\max}}\eta_{p,q} f_r\left(\theta_\parallel, p\Delta v'_\parallel, \theta_\perp, q\Delta v'_\perp, v_\parallel, v_\perp\right), \tag{6}$$

where $p_{\max}$ and $q_{\max}$ may be chosen to be the nearest integers to $v_{\parallel,\max}/\Delta v'_\parallel$ and $v_{\perp,\max}/\Delta v'_\perp$, respectively.

Equation (6) indicates that the Maxwellian ring-beam distribution of equation (2) can potentially serve as the basis of all types of velocity distributions. Unfortunately, equation (6) is not practically useful due to the large number of the ring-beam components involved ($\sim 2p_{\max}q_{\max}$). Note that the order of computational cost is proportional to the number of the ring-beam components multiplied by the cost originated in the numerical approach employed in Paper 1. A preliminary examination shows that at least 2000 ring-beam components are needed to represent the shell distribution in Case II with $\Delta v'_{\parallel} = \Delta v'_{\perp} = 0.1 v_A$, where v_A is the Alfvén speed.

In contrast to the direct approach as suggested by equation (6) which involves a two-dimensional summation, constructing the shell velocity distribution of equation (1) can be done with only a one-dimensional summation. By requiring $\theta_{\parallel} = \theta_{\perp} = \theta$ and $v_d^2 + v_r^2 = v_s^2$, f_s in equation (1) can be approximately represented by

$$f_s \approx f_s^{(N)} \equiv \frac{\pi^{3/2}\theta^3}{NC_s} \sum_{j=-Q}^{N+Q} C_r\left(\theta, v_s \sin(jd\phi)\right)\ f_r\left(\theta, v_s\cos(jd\phi), \theta, v_s \sin(jd\phi), v_{\parallel}, v_{\perp}\right), \tag{7}$$

where $d\phi = \pi/N$ and Q is an "overshoot" factor explained later in this section. In equation (7), the shell velocity distribution has been effectively approximated by a series of ring-beam distributions evenly spaced in pitch angle space. Still, smaller θ and larger v_s values require larger N for better accuracy. One can determine the maximum number of ring-beam components $N_{\max}$ such that $\lim_{N\to N_{\max}} |f_s^{(N)} - f_s|/f_s \le \epsilon$ is satisfied with ϵ being a small number set by the desired accuracy. Of more practical importance is of course the relative contribution of each Maxwellian ring-beam component in equation (7). Letting the contribution of the jth Maxwellian ring-beam be η_j and using the fact that f_r is scaled by $1/C_r$, it is straightforward to deduce

$$\eta_j = \frac{C_r\left(\theta, v_s \sin(jd\phi)\right)}{\sum_{j'=-Q}^{N+Q} C_r(\theta, v_s \sin(j' d\phi))}. \tag{8}$$

Then $f_s \approx \sum_j \eta_j f_r(\theta, v_s\cos(jd\phi), \theta, v_s\sin(jd\phi), v_{\parallel}, v_{\perp})$.

With the same shell parameters, $v_s = 2v_A$ and $\theta = 0.45v_A$, as Case II in Paper 2, Figure 1 displays comparison between the exact (equation (1)) and approximate (equation (7)) shell velocity distributions when $N = 9$ (left column) and $N = 18$ (right column). Note that only the first quadrant (i.e., for $0° \le \alpha \le 90°$, where α is the pitch angle) is displayed since both f_s and $f_s^{(N)}$ are an even function of $v_{\parallel}$. It appears from the figure in the first row that $f_s^{(9)}$ is already a reasonable approximation and the difference between f_s and $f_s^{(18)}$ is indistinguishable. The figures at the bottom row show $f_s^{(N)}$ at the speed of $v = v_s$ (i.e., along the crest of the shell). For the $N = 9$ case (red-dashed curve in Figure 1c) the regularly-spaced ripples are visible due to the coarsely spaced ring-beam components (gray-thin curves represent individual contributions of the Maxwellian ring-beams), but for the $N = 18$ case, these ripples vanish (red-dashed curve in Figure 1d), indicating convergence.

The dotted black curves in Figures 1c and 1d, respectively, represent $f_s^{(9)}$ and $f_s^{(18)}$ with $Q = 0$ in equation (7). Without the overshoot factor, an artificial loss cone is introduced, effect of which can be significant. The appearance of the loss cone is due to $v_s d\phi < \sim 2\theta_s$ for both cases, especially for larger N. Therefore, the missing, nonnegligible contributions to $\phi = 0°$ (or $\phi = 180°$) from the outskirts of the ring-beams immediately below 0° (or above 180°) should be compensated by adding extra ring-beam components with negative ring speeds (doing so is physically nonsense but does not invalidate mathematics). Here, we have simply defined the factor $Q = \mathrm{RND}(2\sqrt{\log 2}\theta/(v_s d\phi))$ to be the ratio of the full width at half maximum of the Maxwellian ring-beam to the spacing of two adjacent ring-beam peaks along the crest of the shell, where RND is the rounding function. The Q values for $N = 9$ and $N = 18$ are in this case 1 and 2, respectively.

The dispersion solver used here is a direct implementation of the formulation provided by Paper 1, which is not only appropriate for the model with the bi-Maxwellian distributions but is also generalized to the Maxwellian ring-beam distributions of equation (2). We shall refer interested readers to Paper 1 for the detailed derivation and guidance to the implementation. For the rest of the paper, by "dispersion solver" we shall, if not explicitly stated, mean the computer program that solves the fully kinetic dispersion equation for Maxwellian ring-beam distributions combined with, as a pre-process, the approximation procedure of a shell distribution as a finite series of Maxwellian ring-beam components. Note that the approximation

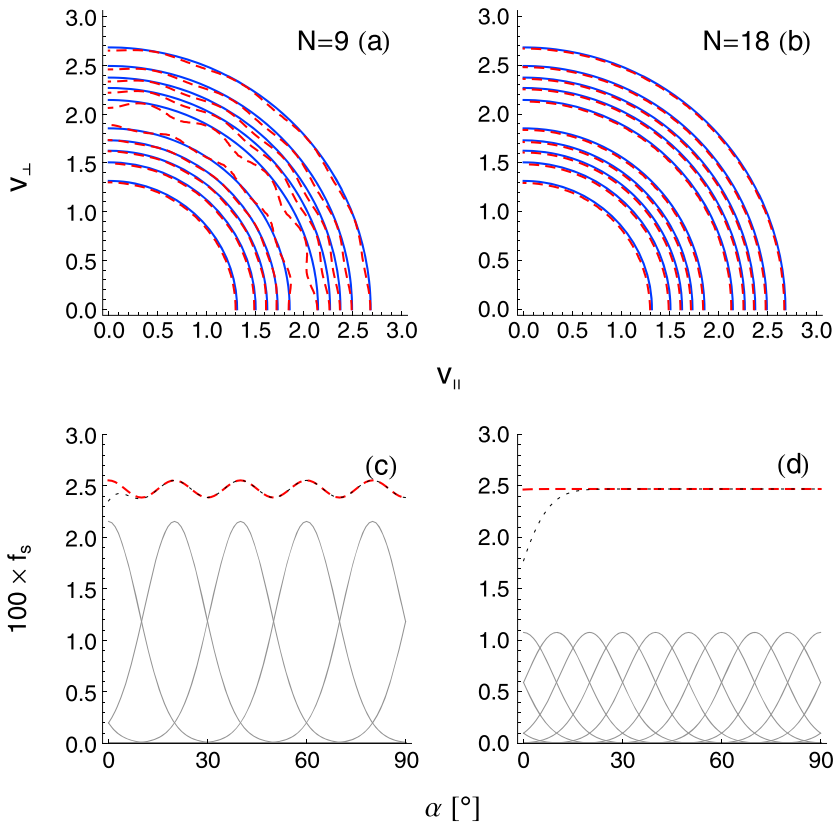

Figure 1. Comparison of the convergence of the approximate shell distributions from equation (7) between (left) $N = 9$ and (right) $N = 18$ cases. Top panels show two dimensional contours of the exact (solid contours) and approximate (dashed contours) shell distributions. (bottom) One-dimensional cut of the approximate (dotted and dashed curves) shell distributions along a quarter of the circle $v_{\parallel}^2 + v_{\perp}^2 = 4$. The solid curves represent contributions from the individual ring-beam components.

procedure is not part of the program, so we apply equation (8) to the shell distribution in advance and use the superimposed ring-beam distributions as inputs to the program.

3. Validation for Subtracted Maxwellian Velocity Distribution

As a first step, we calculate the fully kinetic linear instability driven by the subtracted Maxwellian velocity distribution using the same parameters as Case I of Paper 2. The purpose of this section is twofold: (1) to verify the newly implemented dispersion solver against the well-established dispersion solver based on bi-Maxwellian velocity distributions [*Gary*, 1993] and (2) to establish a quantitative comparison analysis between the linear theory dispersion relation and the simulated waves. Then in section 4 the same comparison analysis will be used to verify the calculation of the ion Bernstein instability driven by the general shell velocity distribution of Case II.

For $v_r = 0$, the Maxwellian ring-beam velocity distribution in equation (2) reduces to the well-known bi-Maxwellian velocity distribution. Case I of Paper 2 used a subtracted Maxwellian proton velocity distribution of the form $f_I = \eta_1 f_r(\theta_{\parallel,1}, 0, \theta_{\perp,1}, 0) - \eta_2 f_r(\theta_{\parallel,2}, 0, \theta_{\perp,2}, 0)$ with the parameters: $\eta_1 = 6.3$, $\theta_{\parallel,1} = \theta_{\perp,1} = \sqrt{0.8} v_A$, $\eta_2 = 5.3$ and $\theta_{\parallel,2} = \theta_{\perp,2} = \sqrt{0.9}\theta_{\parallel,1}$. Electrons had a Maxwellian distribution with $\theta_e/\theta_{\parallel,1} = 0.1$, where θ_e is the electron thermal speed. We here adopt the same parameters, including the reduced proton-to-electron mass ratio of 100 and the relatively small proton plasma-to-cyclotron frequency of $\omega_{pp}/\Omega_{cp} = 15$, to be consistent with simulations in Paper 2 as well as to reduce the simulation cost in the present study.

Figure 2 displays the linear theory growth rate as a function of wave normal angle (ψ) and wave number (k) normalized to the proton inertial length ($\lambda_p = c/\omega_{pp}$), where c is the speed of light, and can be directly compared with Figure 3 of Paper 2. As will be shown in Figure 5, there are a number of dispersion surfaces, most of which are heavily damped ($\gamma < -0.1\Omega_{cp}$). Therefore, in order to construct the 2-D map of growth

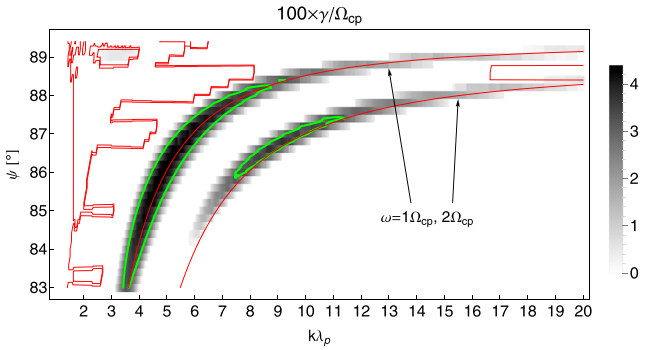

Figure 2. Linear theory growth rate (γ) as a function of the wave number (k) and the wave normal angle (ψ) for Case I. The thin red contours represent real frequencies at $1\Omega_{cp}$ and $2\Omega_{cp}$. The thick green contours represent the $\gamma = 0.03\Omega_{cp}$ level.

rate in Figure 2, we have picked the maximum growth rate across all possible dispersion surfaces for each wave number bin of width $\Delta k\lambda_p = 0.02$, representing the maximum growth rate among all identified dispersion surfaces. Our result shows that, for waves of the first harmonic ($\omega \approx 1\Omega_{cp}$; the dark patch at smaller k), $\gamma_{max} = 0.044\Omega_{cp}$ (local maximum growth rate) at $k\lambda_p = 4.9$ and $\psi = 86.1°$, and for waves of the second harmonic ($\omega \approx 2\Omega_{cp}$; the dark patch at larger k), $\gamma_{max} = 0.035\Omega_{cp}$ at $k\lambda_p = 9.1$ and $\psi = 86.8°$, which are in excellent agreement with the result of Paper 2.

To further validate the linear dispersion analysis results, a series of 1-D PIC simulations using the same simulation code as Paper 2 have been performed. As illustrated in Figure 3, the 1-D simulation domain is along the y axis which is nearly perpendicular to the background magnetic field lying in the x-y plane. Accordingly, the system only allows waves propagating along the y axis with a prescribed wave normal angle ψ. Since waves are expected to grow in the wave normal angle range between 83° and 88° as suggested by Figure 2, we here carry out six individual simulations corresponding to six equally-spaced wave normal angles between 83° and 88°. The other simulation parameters are: simulation domain size $L_y = 126\lambda_p$, 4800 cells, 48,000 simulation particles per cell per species, and the simulation time step of $\Delta t\Omega_{cp} = 0.001$. Compared to the 2-D simulation setup in Paper 2, the 1-D simulations here allow a much better spatial resolution. This is desired as waves across a wide range of wave numbers are expected to grow.

Figure 4a shows the electric and magnetic field energy evolution for $\psi = 86°$ for which the first harmonic mode is most unstable. The picture of exponential growth up to $t\Omega_{cp} \approx 110$ followed by saturation and weak damping is consistent with the energy evolution of the 2-D simulation result of Paper 2 (Figure 4 therein). Any minor difference may be due to the different simulation domain setups (1-D versus 2-D). Throughout the paper, we use the x-component of the simulated magnetic field fluctuations (B_x) for analyses because the electric field fluctuations have increasing noise with increasing k. Note for $\psi \geq 80°$ that B_x is a good proxy to the compressional component of the magnetic field fluctuations ($B_\parallel$) which dominates the transverse components [e.g., *Gary et al.*, 2010].

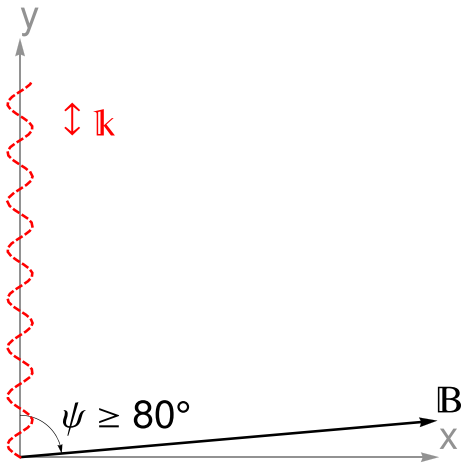

Figure 3. A schematic diagram of the 1-D (along the y axis) simulation domain. The black solid line and red dashed curve represent the background magnetic field vector and wave propagation (along the y axis), respectively.

Figure 5 (top) displays the power spectrum of the simulated waves (B_x^2) as a function of the real frequency and wave number for $\psi = 86°$, and superimposed on that is the linear theory real frequency. To calculate the wave spectrum, we choose the simulated field fluctuations between $t\Omega_{cp} = 20$ and $t\Omega_{cp} = 140$, which corresponds to the linear growth and early steady state phase (Figure 4a), to perform fourier transform. As stated earlier, $\psi = 86°$ roughly corresponds to the local maximum growth rate of the first harmonic mode. The linear dispersion analysis shows that there are numerous dispersion surfaces evidenced by many dispersion curves, although damping is dominant for most of the surfaces (dotted curves versus solid curves). The enhanced wave power from the simulation is aligned excellently with the linear theory dispersion curves that have weak damping or positive wave growth. Especially, waves near the first and second harmonic frequencies are most pronounced and, compared to the cold plasma dispersion relation for fast magnetosonic waves (blue

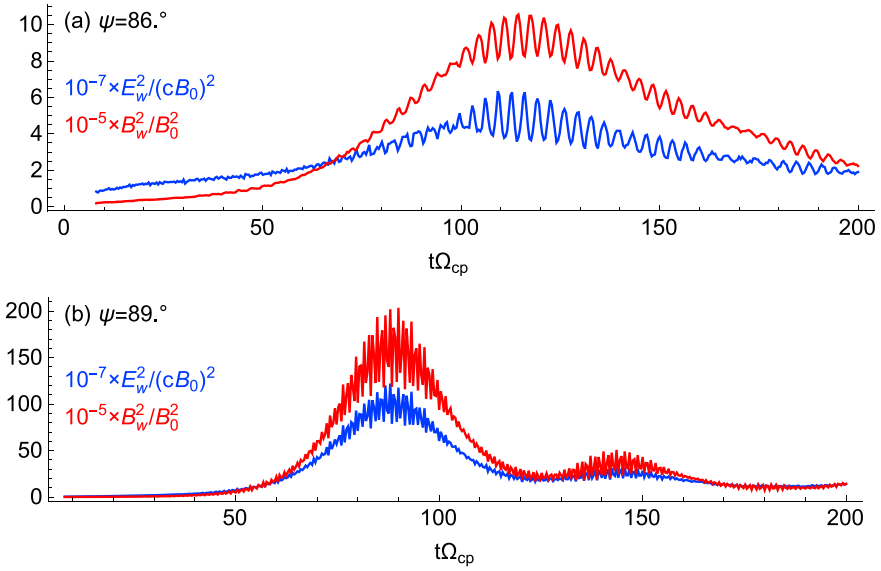

Figure 4. Simulated electric (blue) and magnetic (red) field energy evolution shown in the linear scale for (a) Case I and (b) Case II, corresponding to the wave normal angles of $\psi = 86°$ and $\psi = 89°$, respectively.

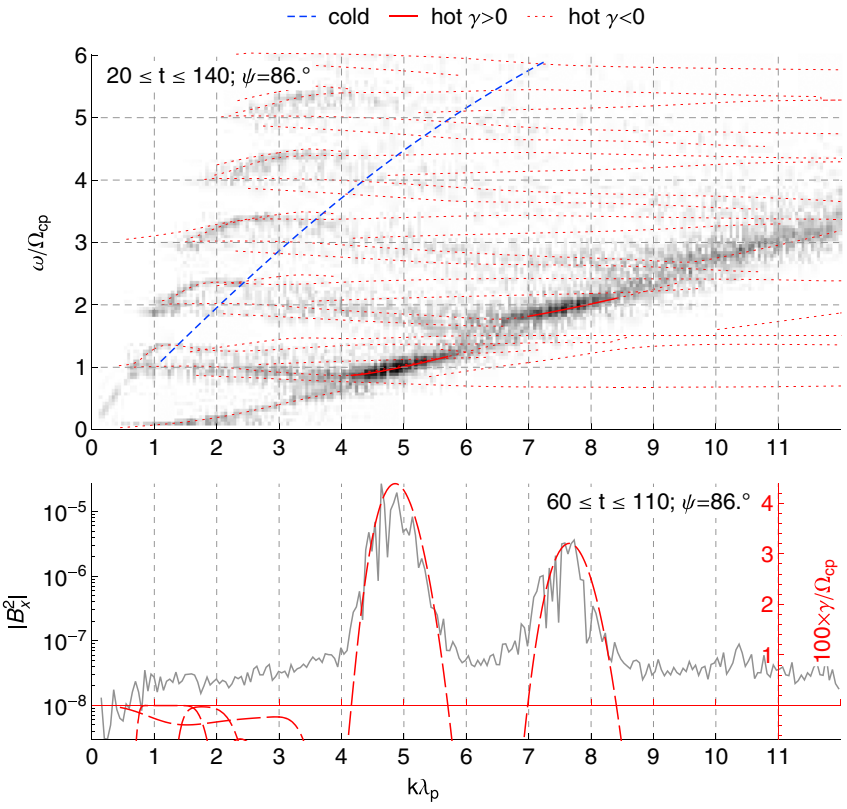

Figure 5. Results for $\psi = 86°$ of Case I. (top) Comparison between the linear theory real frequencies (red dotted and solid curves) and simulated wave power (grayscale image) as a function of the real frequency and wave number. The blue dashed curve represents the cold plasma dispersion curve for fast magnetosonic waves. The red solid (dotted) curves correspond to growth (damping). (bottom) Comparison between the linear theory growth rate (dashed curve with linear scale on the right axis) and the simulated wave power (solid curve with logarithmic scale on the left axis) as a function of the wave number.

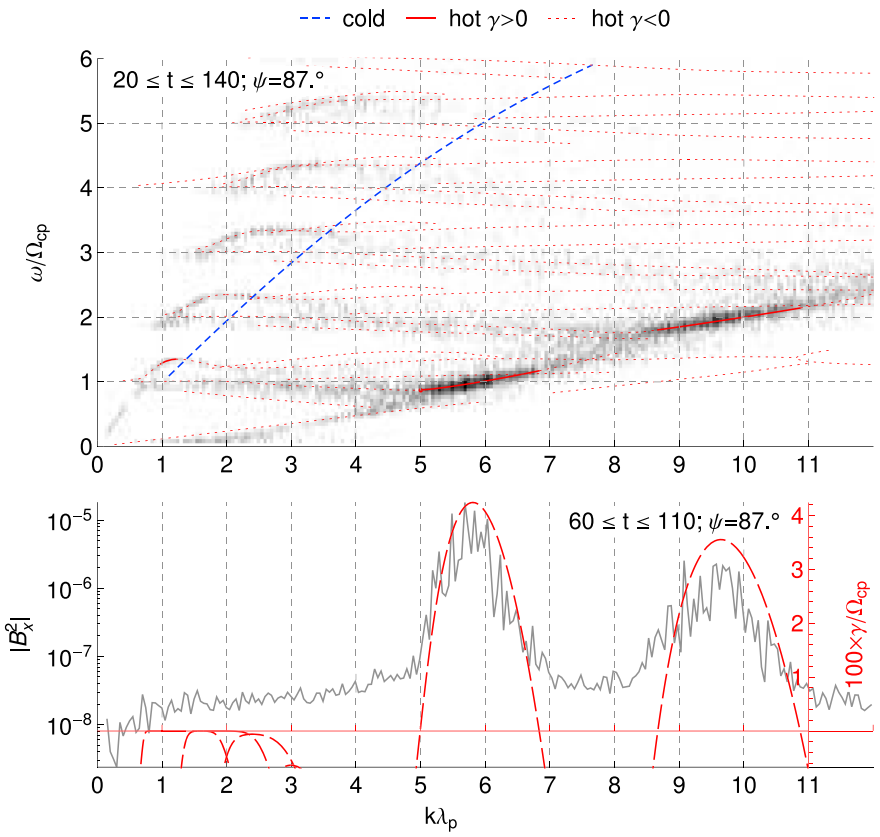

Figure 6. Same as Figure 5, but for $\psi = 87°$.

dashed curve), have much smaller phase speeds (ω/k). The bottom panel shows the comparison between the linear theory growth rate (red dashed curves) and time-averaged wave power (gray solid curve) during the end of the linear growth phase ($60 \le t\Omega_{cp} \le 110$). As expected from the top panel, two peaks of the enhanced waves appear at the wave numbers predicted by the linear theory instability and the widths of the peaks are remarkably consistent with those of the growth rates of the two harmonic modes. The first harmonic ($\omega \approx 1\Omega_{cp}$) which has the strongest wave power appears at $k\lambda_p$ ~4.9, while the second harmonic ($\omega \approx 2\Omega_{cp}$) appears at $k\lambda_p$ ~7.8.

Figure 6, displaying the same quantities as Figure 5 but for $\psi = 87°$, further confirms the excellent agreement between the linear dispersion analysis and the simulation. $\psi = 87°$ roughly corresponds to the local maximum growth rate of the second harmonic. Compared to Figure 5, the enhanced waves at the first and second harmonics moved to larger wave numbers for $\psi = 87°$, deviating further away from the cold plasma dispersion curve. This is also apparent from Figure 2. From the bottom panel, the first and second harmonics of the simulated waves for $\psi = 87°$ appear at $k\lambda_p$ ~5.8 and $k\lambda_p$ ~9.6, respectively, consistent with the linear theory growth rates. The widths of the two harmonic modes are also consistent, although the simulated waves for the second harmonic mode is slightly more spread, likely due to the larger noise level at the larger wave number. The consistent picture of the comparisons for $\psi = 86°$, $\psi = 87°$ and other wave normal angles not shown suggests that the calculations and simulations are in excellent agreement.

4. Full Dispersion Relation for General Shell Velocity Distribution

In this section, we calculate the fully kinetic linear instability driven by the shell velocity distribution using the same parameters as Case II of Paper 2. Here, the subtracted Maxwellian distribution cannot be used. As described in section 2, this shell distribution is approximated with multiple ring-beam distributions using equation (7). To prove such an approximation is legitimate and results in valid instability estimates, we perform a series of 1-D PIC simulations as in the previous section.

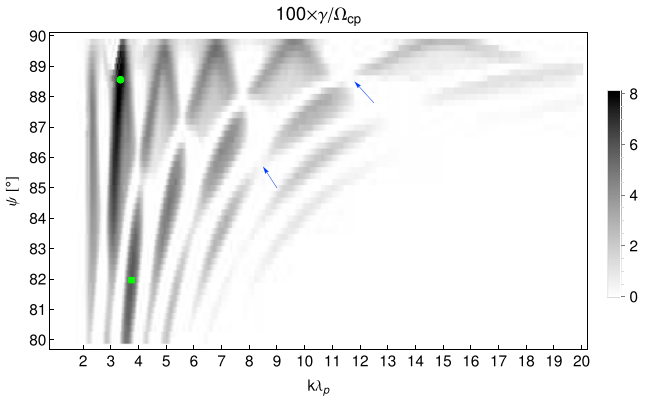

Figure 7. Linear theory growth rate (γ) as a function of the wave number (k) and the wave normal angle (ψ) for Case II. The filled green circle denotes the maximum growth rate of $\gamma = 0.081\Omega_{cp}$ located at $\psi = 88.6°$ and $k\lambda_p = 3.35$. The filled green square denotes the second local maximum growth rate of $\gamma = 0.059\Omega_{cp}$ located at $\psi = 82°$ and $k\lambda_p = 3.75$. Two arrows indicate the growth rate gaps for the $\omega \sim 7\Omega_{cp}$ mode.

The proton populations used in Case II consist of tenuous ($\eta_1 = 0.1$) energetic protons forming a shell distribution of equation (1) with the shell speed $v_{s,1} = 2v_A$ and the thermal spread of the shell $\theta_1 = 0.45v_A$, and dense ($\eta_2 = 0.9$) cold background protons forming the Maxwellian distribution with the thermal speed $\theta_2 = 0.045v_A$. In other words, the proton velocity distribution has the form of $f_{II} = \eta_1 f_s(\theta_1, v_{s,1}) + \eta_2 f_s(\theta_2, 0)$. Electrons form the same Maxwellian velocity distribution as in Case I.

The tenuous shell proton distribution is approximated using equation (7) with $N = 18$, and Figure 7 displays the linear theory growth rate in the same format as Figure 2 (comparison with the $N = 9$ case is discussed in section 5). Here, the wave normal angle spans from 80° to 89.8° in steps of 0.2°. The maximum growth rate is $0.081\Omega_{cp}$ appearing at $k\lambda_p \approx 3.35$ and $\psi \approx 88.6°$ (filled green circle) with $\omega = 2.96\Omega_{cp}$, and the second local maximum growth rate is $0.059\Omega_{cp}$ at $k\lambda_p \approx 3.75$ and $\psi \approx 82°$ (filled green square) with $\omega = 3.60\Omega_{cp}$. Note also that the maximum growth rate for Case II is roughly twice as large as that of Case I. Compared to Figure 2, the overall growth rate pattern is much more complex than Case I and there are more than two harmonic modes at a given wave normal angle that are unstable. One noticeable feature is that the single peak of growth rate appearing at, for example, $k\lambda_p \approx 5$ (4th harmonic mode) and $\psi \approx 89.6°$ immediately splits into two local peaks at both sides of $k\lambda_p \approx 5$ as ψ decreases. The two peaks

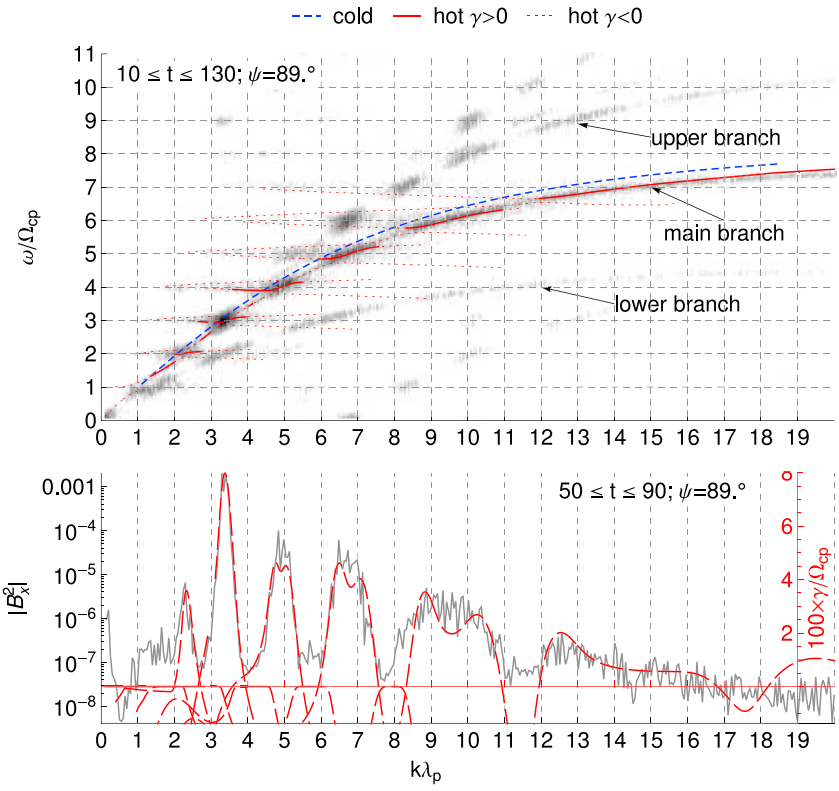

Figure 8. Same as Figure 5, but for $\psi = 89°$ of Case II.

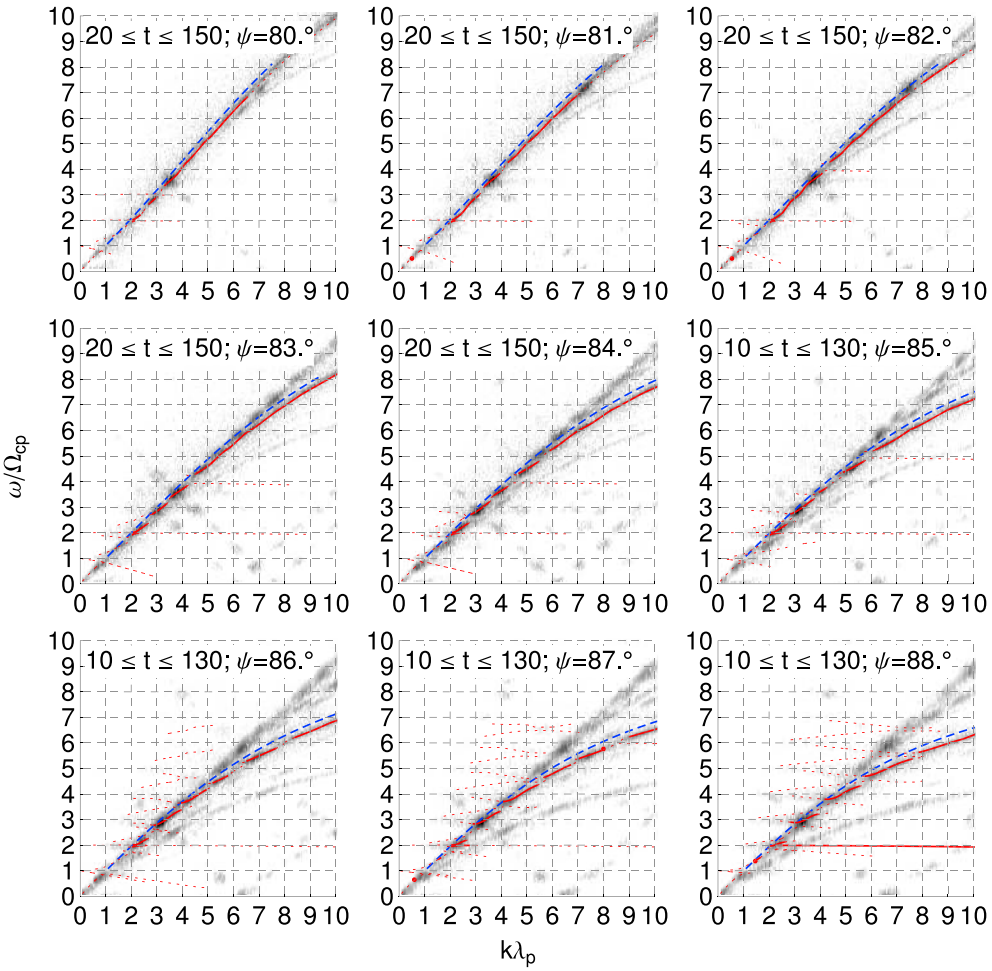

Figure 9. Same as that in Figure 8 (top), but for nine other wave normal angles.

correspond to frequencies below and above $4\Omega_{cp}$, forming a local minimum of the growth rate as a function of frequency at $4\Omega_{cp}$. The same growth rate pattern of splitting peaks appears at higher harmonics as will be further discussed in section 5 (Figure 13). Furthermore for each wave mode, there exist narrow damping gaps (two at most) at intermediate wave normal angles (e.g., refer to the arrows), as opposed to the monotonic increase followed by the monotonic decrease of growth rate with wave normal angle for Case I. To the best of our knowledge, such complexity in the instability pattern driven by the shell distribution have not been previously reported.

To confirm the linear dispersion analysis results, a series of 1-D PIC simulations are carried out. We keep all other simulation parameters identical to the runs for Case I, except that only 5000 simulation particles per cell are used to represent the energetic shell protons, the background protons, and the electrons, respectively. Fewer simulation particles per cell have been used for these runs, associated with the larger linear theory growth rate than that of Case I (see Figures 2 and 7). In addition, as the analysis suggests that waves can be driven substantially unstable for wave normal angles as low as 80°, we accordingly carry out 10 simulations corresponding to the wave normal angles equally spaced between 80° and 89°. Figure 4b shows the electric and magnetic field energy evolution for $\psi = 89°$. Note that the maximum growth rate occurs for $\psi = 88.6°$. Compared to Case I, the waves saturate at larger amplitude but at an earlier time.

Figure 8 displays the dispersion analysis and simulation comparison for $\psi = 89°$ in the same format as Figure 5. In Figure 8 (top), fluctuations are visible in at least three distinct branches (labeled as upper, main, and lower branches in the figure), while the dispersion analysis only predicts the main branch. The cold plasma dispersion curve, represented by the blue dashed curve, is now located very close to the unstable segments of the linear theory dispersion curves and the main branch with only slight deviation. In Figure 8

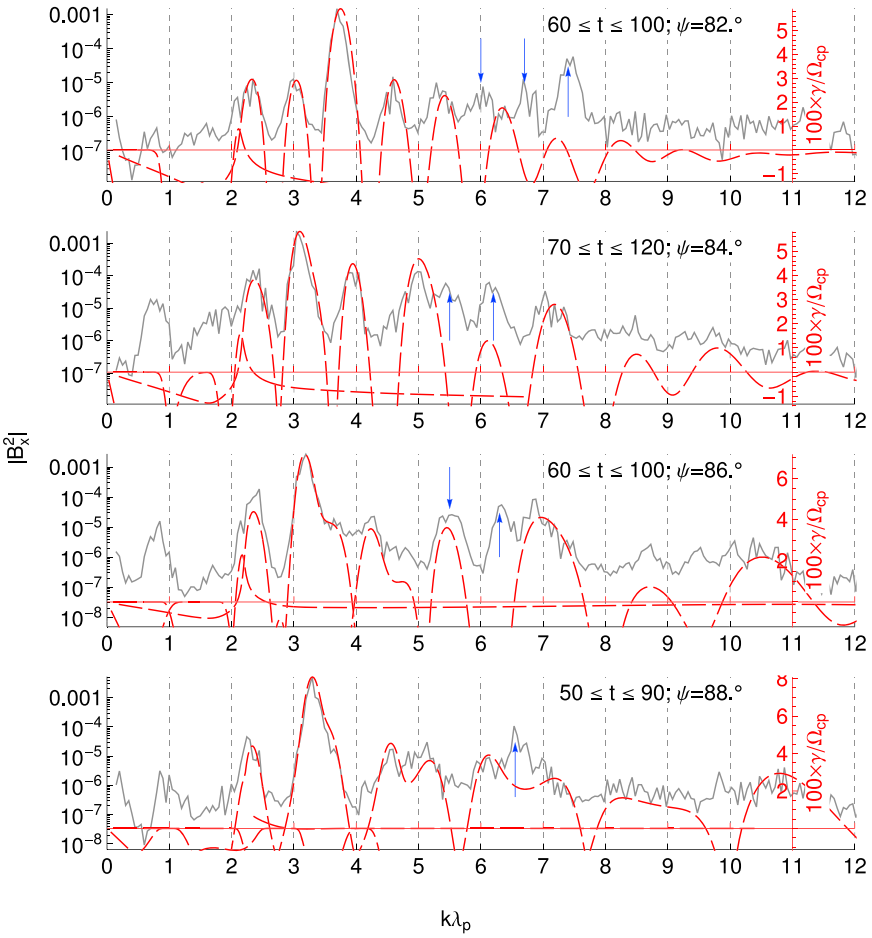

Figure 10. Same as Figure 8 (bottom), but for all the even wave normal angles simulated. Arrows denote the peaks that are dominantly contributed by fluctuations in the upper branch and do not match the linear theory growth rate peaks.

(bottom), the linear theory growth rates and the simulated wave power are compared. Despite the fact that the solutions for the two other branches are not found, the agreement is fairly good. This is because the simulated waves in the main branch dominate. Note though that the contribution of the upper branch above the fourth harmonic mode is noticeable. This picture is different for the other propagation angles as will be shown in the next paragraph. In addition, the simulation shows the strongest third harmonic waves, consistent with the growth rate calculation. Finally, it is worth mentioning that the simulation noise becomes significant for the small amplitude waves at larger *k*.

Figure 9 displays the linear theory real frequencies superimposed on the simulated wave power spectra for all other wave normal angles and demonstrates how the wave dispersion relations vary with the wave normal angle. Our linear theory calculation consistently predicts the main branch of the simulated waves at all other wave normal angles, but none of the other two branches. The other two branches gradually merge into the main branch as the wave normal angle decreases. Figure 9 also shows that, as the wave normal angle decreases, the disconnected dispersion surfaces once present at the large wave normal angles merge into a continuum starting from large *k*, similar to the result of *Horne et al.* [2000].

Figure 10 displays comparison between the simulated wave power and linear theory growth rate for the even wave normal angles simulated. The agreement is fairly good for the first four growth rate peaks (up to the fifth harmonic frequency), but beyond that the waves of the upper branch become significant. The arrows in the figure denote the peaks with substantial contributions from the upper branch. In the next section, we further explore the unexpected upper and lower branches.

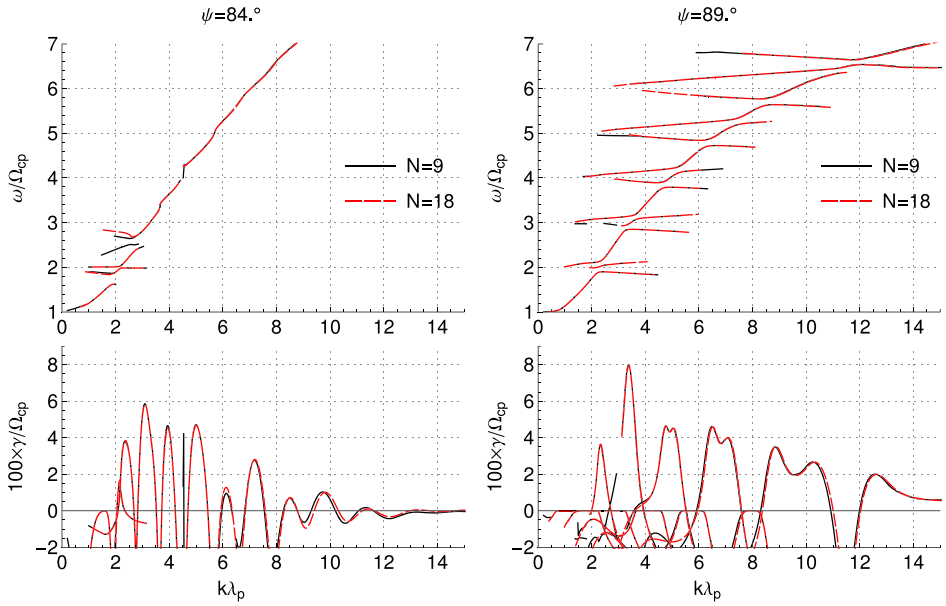

Figure 11. Linear theory comparison of the complex frequency between $N = 9$ (solid curves) and $N = 18$ (dashed curves) cases for (left) $\psi = 84°$ and (right) $\psi = 89°$. (top) Real and (bottom) complex parts as a function of the wave number.

5. Summary and Discussions

We have developed a fully kinetic dispersion solver which approximates a shell velocity distribution using multiple Maxwellian ring-beam velocity distributions for which numerical calculation of the full dispersion relation has been developed [*Umeda et al.*, 2012]. Applying this technique to the two proton shell distributions examined by *Liu et al.* [2011], we have validated the new dispersion solver against first a dispersion solver based on bi-Maxwellian distributions and then PIC simulations. Particularly for Case II in *Liu et al.* [2011], we have shown that the approximate shell distribution converges between $N = 9$ and $N = 18$ (equivalently, between 12 and 23 ring-beam components). To further test the convergence of the linear theory instability, we have performed the same calculation for $N = 9$. Figure 11 compares the linear theory instabilities between the $N = 9$ (solid curves) and $N = 18$ (dashed curves) cases for the selected wave normal angles, 84° and 89°. As is clear from the comparison, the complex frequencies are nearly identical, except for some small deviation in the imaginary parts above $k\lambda_p \approx 8$. Thus, the linear theory instability already converges with $N = 9$ with reasonable accuracy. We have further compared the linear theory instability with simulated waves from 1-D simulations using the exact shell distribution. On the one hand, our dispersion analysis has excellent agreement to the main branch of the simulated waves. On the other hand, the simulations show two extra branches of fluctuations, for which our new dispersion solver could not find any solution.

The two extra branches revealed by the simulations in section 4 are unlikely to be simulation artifacts. Instead, they start to emerge at a later phase of wave growth ($t\Omega_{cp} \sim 70$) and become stronger during the saturation and weak damping phase, perhaps a result of nonlinear interactions. We have carefully repeated these simulations with different simulation parameters. We have varied the simulation domain size, the number of grids, the number of simulation particles, and the simulation time step while keeping other parameters fixed, but the extra branches persistently appear in the simulation results (not shown). These extra branches seem to be a unique feature related to the shell-type velocity distributions instead. We have carried out a number of simulations with different shell parameters and even with different types of distributions. We present only three cases for the propagation angle of 89°. In the first run ($\mathcal{R}1$), we replaced the shell component with a Maxwellian distribution of the same effective temperature (i.e., plasma beta $\beta_1 = 4\eta_1$). In the second run ($\mathcal{R}2$), we reduced the shell speed $v_{s,1}$ from $2v_A$ to $1.4v_A$ and increased the shell concentrations η_1 from 0.1 to 0.2. In the last run ($\mathcal{R}3$), we replaced the shell component with a non-drifting single Maxwellian ring whose ring speed and concentration are $2v_A$ and 0.05, respectively (the concentration of 0.05 keeps the linear instability growth rate in the same order as Case II). Figure 12 shows the results of the three runs in the same format as that in Figure 5 (top). For $\mathcal{R}1$, the two extra branches disappear and the simulated fluctuations are organized along the predicted dispersion curves (note that the system is

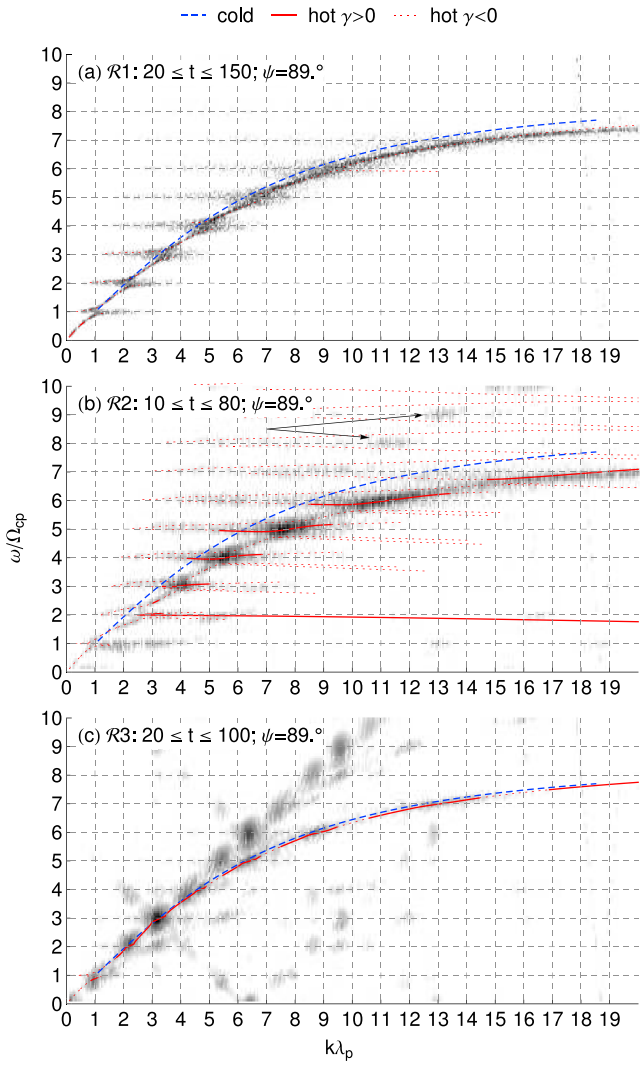

Figure 12. Three simulation runs with different energetic proton distributions for $\psi = 89°$ to further explore the unexpected upper and lower branches shown in Figure 8a (the conditions of cases $\mathcal{R}1$, $\mathcal{R}2$ and $\mathcal{R}3$ are described in the text). The figure format is same as that in Figure 5 (top).

stable in this run evidenced by no positive growth rate). For $\mathcal{R}2$, i.e., with the reduced shell speed, the lower branch is almost completely suppressed, the upper branch (denoted by arrows) is weakened substantially, and the main branch follows the linear theory dispersion curves. For $\mathcal{R}3$, there appear a strong upper branch and weak lower branch. Interestingly, these features are similar to Case II examined (Figure 8), although the relative amplitudes are different. Again, the main branch follows the predicted dispersion curves. According to these results, it appears that the waves following the extra branches are not simulation artifacts but rather related to the ring- and shell-type distributions with a large ring and shell speed. Future investigation is certainly needed to examine the origin of these extra wave branches.

One drawback of our approach is the computational cost as briefly stated in section 2. There are two factors contributing to this. First, numerical integration to evaluate integrals involving the ring-beam velocity distribution functions is costly. Second, this numerical integration has to be done with the individual ring-beam components used in equation (7) ($N + 2Q + 1 = 23$ components for the analysis in section 4). For instance, calculation of the dispersion relation with $\Delta k\lambda_p = 0.01$ for a single wave normal angle (e.g., Figure 8) took near an hour, compared to several tens of minutes for Case I (e.g., Figure 5), on a single core of 3.2 GHz clock speed of a quad-core desktop. Note that there are many more dispersion branches in Case I.

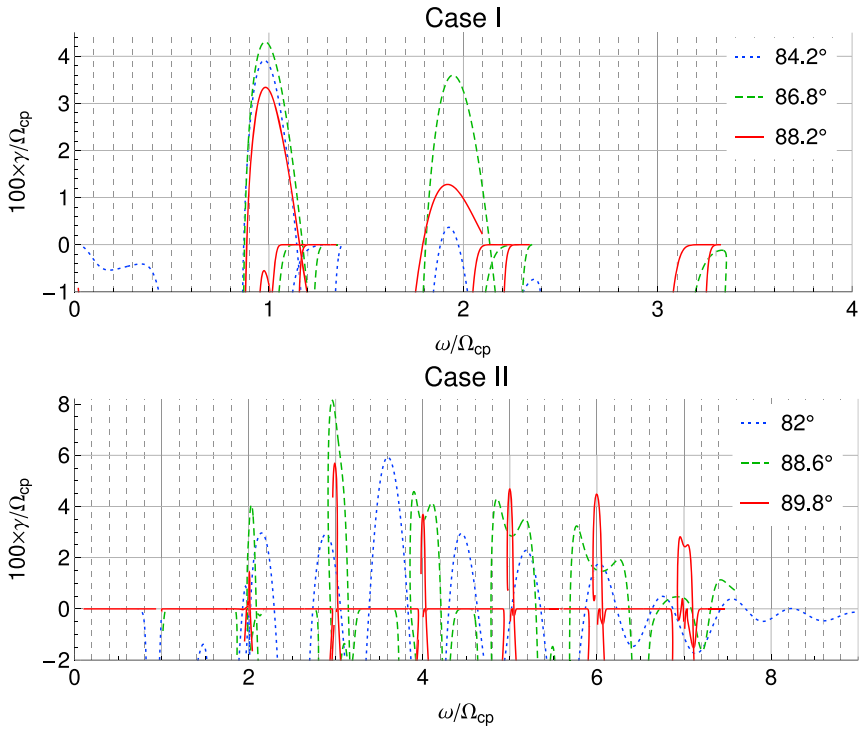

Figure 13. Linear theory growth rates as a function of the real frequency for (top) Case I and (bottom) Case II. The three curves in each panel correspond to growth rates for three different wave normal angles as denoted by the legends.

One comparison that is of particular interest to the observational studies of fast magnetosonic waves is given in Figure 13 which displays growth rates as a function of frequency for the two cases examined. For Case I (top), two peaks occur nearly at the first two harmonics of Ω_{cp} ($0.99\Omega_{cp}$ and $1.92\Omega_{cp}$, respectively) almost independent of the wave normal angles. This is clearly shown in Figure 2 where two local maxima of growth rates are aligned very well with the $\omega = 1\Omega_{cp}$ and $2\Omega_{cp}$ contours. But for Case II (bottom), the peaks appear at the integer multiples of Ω_{cp} only if the propagation direction is nearly perpendicular to the background magnetic field. At $\psi = 88.6°$, growth rates start to be slightly suppressed at $4\Omega_{cp}$, $5\Omega_{cp}$ and $6\Omega_{cp}$ (the feature of splitting peaks discussed in section 4), and as a result, two local maxima appear at both sides of each integer harmonic frequency. This picture is very different from instabilities driven by the nondrifting Maxwellian ring velocity distribution examined by *McClements et al.* [1994] (Figure 4 therein) whose analyses showed that around each harmonic there exists only a single local maximum of growth rate for all wave normal angles examined. Indeed, our dispersion analysis for a nondrifting single Maxwellian ring as in $\mathcal{R}3$ discussed above gives similar results as in *McClements et al.* [1994]. More interestingly at $\psi = 82°$, the peaks not only occur far from the integer multiples of Ω_{cp} but are somewhat irregularly spaced (i.e., the frequency spacings slightly vary for every pair of the nearby peaks). Since the peak near $3.6\Omega_{cp}$ at $\psi = 82°$ is the second largest (also shown in Figure 7), this wave mode is likely to grow as strongly as the ones occurring at the integer harmonics of Ω_{cp} at more perpendicular propagation angles. This result is somewhat different from the conventional view of fast magnetosonic wave excitation, whereby strong magnetosonic waves are excited at the harmonics of the proton cyclotron frequency at the propagation direction nearly perpendicular to the background magnetic field [e.g., *Chen et al.*, 2010] and any waves with spectral peaks not located at the exact harmonics of the proton cyclotron frequency may have been propagated radially from other locations where they are excited [e.g., *Perraut et al.*, 1982; *Santolík et al.*, 2002; *Ma et al.*, 2014]. Thus, our result suggests another possibility that waves can locally grow at frequencies away from integer harmonics of the proton cyclotron frequency (at wave normal angles sufficiently away from the perpendicular direction).

The appearance of the growth rate peaks at the nonintegral harmonics of Ω_{cp} for oblique propagation sufficiently away from the perpendicular direction is also presented for the Maxwellian ring velocity distribution in *McClements et al.* [1994] (Figure 4 therein) and these authors explained that this is due simply to the differential Doppler shift introduced by the finite parallel velocity spread of the ring. It is likely that the

complex structure of growth rates shown in Figure 7 is due to the same reason, but what makes the structure more complicated than that of the Maxwellian ring distribution presented in *McClements et al.* [1994] is the extended parallel velocity spread and nonmonotonic $\partial f_s(v_\parallel, v_\perp)/\partial v_\parallel$ due to the shell structure with the large shell velocity.

The unstable waves in Case I are far away from the cold plasma dispersion curve as shown in Figures 5 and 6. These waves are clearly ion Bernstein waves. In Case II, however, the unstable waves are close to the cold plasma dispersion curve (Figures 8 and 9). The waves then become fast magnetosonic like. The contrast between the two cases reveals a regime transition of the instability associated with several parameters of the shell velocity distribution, such as the relative density of the shell ions and the shell speed. This regime transition has been briefly discussed in *Liu et al.* [2011], but the investigation was limited because there was no dispersion solver for shell velocity distributions available. The new dispersion solver developed here will enable us to closely examine the regime transition.

Acknowledgments

Data supporting Figures 2 and 4–9 are available upon request from the corresponding author. The work at Auburn University was supported by NASA grant NNX13AD62G and NSF grant 1303623. Computational resources supporting this work were provided by the NASA High-End Computing (HEC) Program through the NASA Advanced Supercomputing (NAS) Division at Ames Research Center. Authors are grateful to S. Peter Gary for his constructive comments and Xueyi Wang for his insights into the two extra branches from simulation.

Larry Kepko thanks S. Gary and another reviewer for their assistance in evaluating this paper.

References

Arfken, G. B., H. J. Weber, and F. E. Harris (2013), Mathematical Methods for Physicists, 7th ed., Academic Press, Boston, doi:10.1016/B978-0-12-384654-9.00011-6.

Boardsen, S. A., D. L. Gallagher, D. A. Gurnett, W. K. Peterson, and J. L. Green (1992), Funnel-shaped, low-frequency equatorial waves, *J. Geophys. Res.*, *97*(A10), 14,967–14,976, doi:10.1029/92JA00827.

Broughton, M. C., M. J. Engebretson, K.-H. Glassmeier, Y. Narita, A. Keiling, K.-H. Fornaćcon, G. K. Parks, and H. Réme (2008), Ultra-low-frequency waves and associated wave vectors observed in the plasma sheet boundary layer by Cluster, *J. Geophys. Res.*, *113*, A12217, doi:10.1029/2008JA013366.

Chen, L., R. M. Thorne, V. K. Jordanova, and R. B. Horne (2010), Global simulation of magnetosonic wave instability in the storm time magnetosphere, *J. Geophys. Res.*, *115*, A11222, doi:10.1029/2010JA015707.

Cottrell, G. A., and R. O. Dendy (1988), Superthermal radiation from fusion products in JET, *Phys. Rev. Lett.*, *60*(1), 33–36.

Dendy, R. O., and K. G. McClements (1993), Ion cyclotron wave emission at the quasi-perpendicular bow shock, *J. Geophys. Res.*, *98*(A9), 15,531–15,539, doi:10.1029/93JA01386.

Denton, R. E., M. J. Engebretson, A. Keiling, A. P. Walsh, S. P. Gary, P. M. E. Décréau, C. A. Cattell, and H. Rème (2010), Multiple harmonic ULF waves in the plasma sheet boundary layer: Instability analysis, *J. Geophys. Res.*, *115*, A12224, doi:10.1029/2010JA015928.

Freund, H. P., and C. S. Wu (1988), Stability of a spherical shell distribution of pickup ions, *J. Geophys. Res.*, *93*(A12), 14,277–14,283, doi:10.1029/JA093iA12p14277.

Gary, S. P. (1993), *Theory of Space Plasma Microinstabilities*, Cambridge Univ. Press, New York.

Gary, S. P., K. Liu, D. Winske, and R. E. Denton (2010), Ion Bernstein instability in the terrestrial magnetosphere: Linear dispersion theory, *J. Geophys. Res.*, *115*, A12209, doi:10.1029/2010JA015965.

Gary, S. P., K. Liu, and D. Winske (2011), Bernstein instability driven by suprathermal protons in the ring current, *J. Geophys. Res.*, *116*, A08215, doi:10.1029/2011JA016543.

Gul'elmi, A., B. Klaine, and A. Potapov (1975), Excitation of magnetosonic waves with discrete spectrum in the equatorial vicinity of the plasmapause, *Planet. Space Sci.*, *23*(2), 279–286, doi:10.1016/0032-0633(75)90133-6.

Horne, R. B., G. V. Wheeler, and H. S. C. K. Alleyne (2000), Proton and electron heating by radially propagating fast magnetosonic waves, *J. Geophys. Res.*, *105*(A12), 27,597–27,610, doi:10.1029/2000JA000018.

Janhunen, P., A. Olsson, A. Vaivads, and W. K. Peterson (2003), Generation of Bernstein waves by ion shell distributions in the auroral region, *Ann. Geophys.*, *21*(4), 881–891, doi:10.5194/angeo-21-881-2003.

Liu, K., S. P. Gary, and D. Winske (2011), Excitation of magnetosonic waves in the terrestrial magnetosphere: Particle-in-cell simulations, *J. Geophys. Res.*, *116*, A07212, doi:10.1029/2010JA016372.

Ma, Q., W. Li, L. Chen, R. M. Thorne, and V. Angelopoulos (2014), Magnetosonic wave excitation by ion ring distributions in the Earth's inner magnetosphere, *J. Geophys. Res. Space Physics*, *119*, 844–852, doi:10.1002/2013JA019591.

McClements, K. G., R. O. Dendy, and C. N. Lashmore-Davies (1994), A model for the generation of obliquely propagating ULF waves near the magnetic equator, *J. Geophys. Res.*, *99*(A12), 23,685–23,693, doi:10.1029/94JA01979.

Meredith, N. P., R. B. Horne, and R. R. Anderson (2008), Survey of magnetosonic waves and proton ring distributions in the Earth's inner magnetosphere, *J. Geophys. Res.*, *113*, A06213, doi:10.1029/2007JA012975.

Perraut, S., A. Roux, P. Robert, R. Gendrin, J.-A. Sauvaud, J.-M. Bosqued, G. Kremser, and A. Korth (1982), A systematic study of ULF waves above f_{H+} from GEOS 1 and 2 measurements and their relationships with proton ring distributions, *J. Geophys. Res.*, *87*(A8), 6219–6236, doi:10.1029/JA087iA08p06219.

Russell, C. T., R. E. Holzer, and E. J. Smith (1970), OGO 3 observations of ELF noise in the magnetosphere: 2. The nature of the equatorial noise, *J. Geophys. Res.*, *75*(4), 755–768, doi:10.1029/JA075i004p00755.

Santolík, O., J. S. Pickett, D. A. Gurnett, M. Maksimovic, and N. Cornilleau-Wehrlin (2002), Spatiotemporal variability and propagation of equatorial noise observed by Cluster, *J. Geophys. Res.*, *107*(A12), 1495, doi:10.1029/2001JA009159.

Umeda, T. (2007), Numerical study of electrostatic electron cyclotron harmonic waves due to Maxwellian ring velocity distributions, *Earth Planets Space*, *59*(11), 1205–1210, doi:10.1186/BF03352068.

Umeda, T., M. Ashour-Abdalla, D. Schriver, R. L. Richard, and F. V. Coroniti (2007), Particle-in-cell simulation of Maxwellian ring velocity distribution, *J. Geophys. Res.*, *112*, A04212, doi:10.1029/2006JA012124.

Umeda, T., S. Matsukiyo, T. Amano, and Y. Miyoshi (2012), A numerical electromagnetic linear dispersion relation for Maxwellian ring-beam velocity distributions, *Phys. Plasmas*, *19*(7), 072107, doi:10.1063/1.4736848.